

Effective Field Theory Approach to Scattering of Dark Matter in XENON100 Detector 225 live days run

We report a WIMP search results in XENON100 detector considering a non-relativistic effective field theory approach. The data from scientific run II (34 kg * 224.6 live days) was re-analyzed extending the energy range to 6.6-240 keV. Background and data are found to be compatible. We present 90% confidence level exclusion limits on the coupling constant of each operator c_i extracted using a binned profile likelihood method. We also consider the case of an inelastic WIMP with more than one mass state scattering and set exclusion limits on this model as well. The presented limits are to date the strongest published limits.

Keywords: Dark Matter, EFT, Xenon

I. INTRODUCTION

Astrophysical and cosmological observations present evidence that 27% of the mass-energy of the Universe is made out of Dark Matter (DM), a non-luminous, non-baryonic and non-relativistic particle, the nature of which is yet unknown [1]. Several well motivated theoretical models extends the Standard Model of particle physics predicting the existence of Weakly Interacting Massive Particles(WIMPs) [2]. This hypothesis is currently being tested by many experiment either indirectly, or directly by measuriring the rare scattering of WIMPs from target nuclei. Although some experiment see an excess for WIMPs in the mass range of 6-30 GeV/ C^2 [3-6], these results are not confirmed by other experiments [7-9].

Typically the approach followed in theoretical computations of WIMP-nucleon scattering is to reduce the type of interactions to Spin Independent (SI) and Spin Dependent (SD) only [10], however this is not exhaustive. In recent years an Effective Field Theory (EFT) approach has been developed [11-13], this takes into account all leading-order and next-to-leading order operators emerging from an effective Lagrangian describing the WIMP-nucleus interaction. In this framework new operators which come from different type of nuclear responses are introduced along with the standard SI and SD ones. The parametrization of the fourteen operators \mathcal{O}_i is listed in Eq. 1 and follows the convention from [12]. The operators depend explicitly on 4 quantities: \vec{v}^\perp , the relative velocity between the WIMP and the nucleon, \vec{q} , the momentum transfer, and the WIMP and nucleon spin \vec{S}_χ , \vec{S}_N . Notice that \mathcal{O}_2 is not considered here as it cannot be obtained from a relativistic operator at leading order.

Unlike the commonly studied types of interaction (SI,SD) which are not suppressed when $\vec{q} \rightarrow 0$ and most of their interaction rate is expected to be in low energies nuclear recoils, some of the fore-mentioned operators depend explicitly on \vec{q} and their interaction cross section is suppressed for low momentum transfers, this results in higher expected nuclear recoil scattering energies, see Figure 1. Typically direct detection experiments base their searches on the SI and SD interaction types, high energy nuclear recoil regions (> 43 keV) remain then unexplored.

Another assumption that can be relaxed is that WIMP should scatter elastically, however there are models in which the incoming and outgoing WIMPs have different mass states [14]. In the case where the outgoing state is more massive than the incoming state the cross section for low recoil energies can again be suppressed. Recently an inelastic adaptation of the EFT operator framework discussed above was developed [15]. The operators presented in 1 are modified such that

$$\vec{v}_{inelastic}^\perp = \vec{v}_{elastic}^\perp + \frac{\delta_m}{|\vec{q}|^2} \vec{q}.$$

$$\begin{aligned}
\mathcal{O}_1 &= 1_\chi 1_N \\
\mathcal{O}_3 &= i \vec{S}_N \cdot \left(\frac{\vec{q}}{m_N} \times \vec{v}^\perp \right) \\
\mathcal{O}_4 &= \vec{S}_\chi \cdot \vec{S}_N \\
\mathcal{O}_5 &= i \vec{S}_\chi \cdot \left(\frac{\vec{q}}{m_N} \times \vec{v}^\perp \right) \\
\mathcal{O}_6 &= (\vec{S}_\chi \cdot \frac{\vec{q}}{m_N})(\vec{S}_N \cdot \frac{\vec{q}}{m_N}) \\
\mathcal{O}_7 &= \vec{S}_N \cdot \vec{v}^\perp \\
\mathcal{O}_8 &= \vec{S}_\chi \cdot \vec{v}^\perp \\
\mathcal{O}_9 &= i \vec{S}_\chi \cdot (\vec{S}_N \times \frac{\vec{q}}{m_N}) \\
\mathcal{O}_{10} &= i \vec{S}_N \cdot \left(\frac{\vec{q}}{m_N} \right) \\
\mathcal{O}_{11} &= i \vec{S}_\chi \cdot \left(\frac{\vec{q}}{m_N} \right) \\
\mathcal{O}_{12} &= \vec{S}_\chi \cdot (\vec{S}_N \times \vec{v}^\perp) \\
\mathcal{O}_{13} &= i (\vec{S}_\chi \cdot \vec{v}^\perp)(\vec{S}_N \times \frac{\vec{q}}{m_N}) \\
\mathcal{O}_{14} &= i (\vec{S}_\chi \times \frac{\vec{q}}{m_N})(\vec{S}_N \cdot \vec{v}^\perp) \\
\mathcal{O}_{15} &= -(\vec{S}_\chi \times \frac{\vec{q}}{m_N})[(\vec{S}_N \times \vec{v}^\perp) \cdot \frac{\vec{q}}{m_N}]
\end{aligned} \tag{1}$$

This EFT framework is constructed at the WIMP-nucleon level and so each operator may be present independently for protons and neutrons, though UV models can of course correlate their couplings. The full EFT thus has 28 coupling parameters plus the WIMP mass, and, in the inelastic case, a mass splitting δ . The parameter

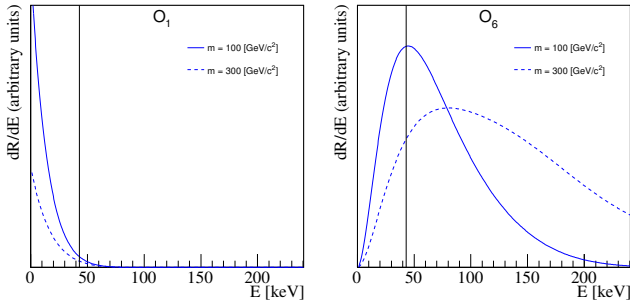


FIG. 1. Example EFT recoil spectra for elastic scattering of spin-1/2 WIMPs on Xenon nuclei (weighted according to the isotope abundances in the XENON100 experiment). Left(right) shows the predicted spectra for EFT operate $\mathcal{O}_1(\mathcal{O}_6)$. The normalization is controlled by the coupling coefficient of each EFT operator and the experimental exposure (left arbitrary in this figure). The solid vertical line at 43 keV shows the approximate division between the two signal regions used in this analysis (30 PE in cS1). As shown, the standard SI (\mathcal{O}_1) spectrum is concentrated mainly in the already explored energy region. However, some EFT operators, for certain WIMP masses, predict a significant fraction of recoil events above the upper energy cut used in the standard spin-independent analysis, motivating an extension of this cut. The highest recoil energy shown in the plots, 240 keV, roughly corresponds to the extended cS1 cut of 180 PE used in this analysis.

space is thus too large to explore in full, so we take a similar approach to the SI/SD case and characterize the experimental limit by assuming only one active operator at a time, with the coupling to protons and neutrons for that operator set equal (the isoscalar case). However, to facilitate the full exploitation of these results by the community, we provide in supplementary material a set of tools for converting any theoretical recoil spectrum dR/dE into an accurate signal prediction for our analysis which can be used to produce the event rate in the detector, including its response and efficiency. This may help to set a mildly conservative but quite accurate limit on arbitrary models in the full EFT parameter space, or indeed any other particle dark matter model for which one has the expected recoil spectrum.

In this paper, motivated by these EFT extensions of the standard WIMP framework, we report on an analysis extending the energy range up to 240 keV for the first time in XENON100 experiment, and present exclusion limits on all operators for both the elastic and the inelastic WIMP cases.

II. THE XENON100 DETECTOR

The XENON100 detector is a cylindrical dual-phase (liquid and gas) xenon time projection chamber (TPC). It is installed at the Laboratori Nazionali del Gran Sasso (LNGS) in Italy and hosts 161 kg of liquid xenon (LXe),

of which 62 kg perform as active target [16]. The detector consists of a total of 178 1-inch square Hamamatsu R8520-AL photomultiplier tubes (PMTs) employed in two arrays, one in the gas phase at the top of the TPC, the other at the bottom, immersed in LXe.

A particle interacting with the LXe deposits energy that creates both excited and ionized molecular states. De-excitation of these excited molecular states induce a prompt scintillation signal (S_1), while electrons from ionization processes are drifted in an electric field of 530V/cm towards the liquid-gas interface where they are extracted using larger electric field of ~ 12 kV/cm. These electrons generate a proportional scintillation, which is called S_2 . The spatial distribution of the S_2 signal on the top PMT array, together with the time difference between S_1 and S_2 provides the X-Y and Z coordinates of the interaction, respectively, and thus a 3D position reconstruction is achieved.

Interactions in different positions cover different solid angles with respect to the PMT array, which leads to a position-dependent S_1 signal, at the same time warping of the top meshes and the absorption of electrons by residual impurities lead to a position-dependent S_2 signal. To take into account these effects a correction is applied based on a light collection efficiency (LCE) map. The corrected signals (cS1,cS2) are spatially independent and uniform to all interactions [16].

The S_2/S_1 ratio is known to differ between nuclear recoil (NR) and electronic recoil (ER) interactions, thus used as discriminating variable between a WIMP signal and ER background. The logarithm of this ratio, $\log(cS2/cS1)$ is referred later in the text as the y discriminating variable.

III. DATA ANALYSIS

In this work we re-analyze scientific run II data recorded between February 2011 and March 2012, corresponding to 224.6 live days. The characterization of the detector response to ER interactions is performed using dedicated calibration campaigns with ^{60}Co and ^{232}Th radioactive sources, while the response to NR interactions is preformed using $^{241}\text{AmBe}$ calibration campaigns.

This work extends the previous results [7, 17], referred to in the following as the low energy channel, with a new study exploring the energy range between 43-240 keV. The data analysis is divided into two mutually exclusive channels, one optimized for low energies and ranging from 3-30 PE in cS1 (lowE), the other optimized for high energies recoils ranging from 30-180 PE in cS1 (highE). These two analysis are finally statistically combined. The relative region of interests (ROI) of these two channels are shown in Figure 3 and further described in the following sections.

142

A. Low Energy

143 This analysis channel relies on the re-analysis of run II
 144 data described in [7]. The region of interest, the back-
 145 ground expectation models, data selections and their ac-
 146 ceptances are mostly unchanged and only briefly sum-
 147 marized here. Differences with respect to said results are
 148 highlighted when present.

149 The region of interest for this channel spans the
 150 ($y, cS1$)-plane and is shown in Figure 3. The lower bound
 151 on y corresponds to the 3σ acceptance quantile (as a
 152 function of $cS1$) of a 20 GeV WIMP mass signal model,
 153 while the upper bound is fixed at $y = 2.7$. The range in
 154 $cS1$ is constrained instead to be within 3 and 30 PE. This
 155 ROI is further divided into WIMP mass dependent sub-
 156 regions (also called bands) arranged in a way to achieve
 157 constant signal density in each region, as described in [7].

158 Other than falling into the ROI, an event should fulfill
 159 several additional selection criteria such as, data quality
 160 and noise cuts, an event veto in presence of energy release
 161 in the outer LXe shield, energy selection and S2 thresh-
 162 old cut, selection of single-scatter event and a predefined
 163 fiducial volume of 34 kg. More details on these selection
 164 criteria and their relative WIMP signals acceptances can
 165 be found in [7, 18]. Furthermore, this analysis channel
 166 uses the post unblinding cuts described in [7]. These ad-
 167 ditional selections consist of a cut targeted to suppress
 168 data periods with non random occurrence of lone-S1 (an
 169 S1 without any correlated S2) and of a data reprocessing
 170 with an improved (S1,S2) classification algorithm. Fi-
 171 nally, this channel does not employ a variable lower S1
 172 threshold as a function of the event position, but a fixed
 173 lower threshold cut on $cS1$ at 3 PE, converse to what was
 174 reported in [7].

175 The expected background is modeled separately for ER
 176 and NR contributions which are then scaled to exposure
 177 and added together. The NR background is estimated
 178 by Monte Carlo simulation and accounts for the radio-
 179 genic and cosmogenic neutrons contributions [19]. The
 180 ER background is parametrized as the superimposition of
 181 a Gaussian-shaped and non-Gaussian components. The
 182 first one is obtained via a parametric fit of the ^{60}Co and
 183 ^{232}Th calibration data, as discussed in [17]. Whereas
 184 the expected distribution and yields for the non-Gaussian
 185 population, consisting of anomalous events such as those
 186 presenting incomplete charge collection or accidental co-
 187 incidence of uncorrelated S1s and S2s, are evaluated em-
 188 ploying dedicated techniques described in [7].

189 Systematic uncertainties on the background model
 190 arising from the Gaussian parametrized fit, from the NR
 191 and the non-Gaussian contributions normalizations have
 192 been evaluated. It has been shown that the propagated
 193 errors are conservatively within the calibration samples
 194 (used to assess the model) statistical uncertainties, thus
 195 chosen as the overall uncertainty of the model [7].

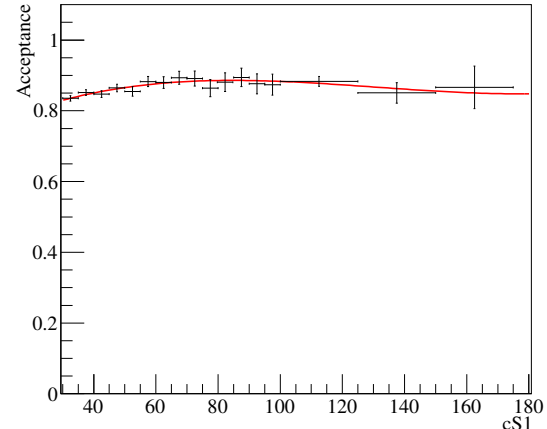


FIG. 2. The total acceptance of all cuts used, data from calibration in black and the fit in red.

196

B. High Energy

197 This analysis channel explores high energy nuclear re-
 198 coils and is the focus of this work. The data selection
 199 criteria described in detail in [18] were optimized for high
 200 acceptance to low energy nuclear recoils. Most of these
 201 selection criteria (cuts) were fully compatible or simply
 202 extended to high energy depositions, however some re-
 203 quired more comprehensive studies and are detailed in
 204 what follows.

205 The width of an S2 pulse increases with the depth (z)
 206 of the interaction. This is due to the diffusion of the
 207 electron cloud during its propagation towards the gate
 208 grid. Low energy S2 events show larger spread due to
 209 low statistics of drifted ionization electrons, hence the
 210 cut was previously defined in an energy-dependent way.
 211 However for energy recoil which are high enough (highE
 212 region) this energy dependency is not valid. We use here
 213 a cut on the S2 width which is a function of the depth
 214 of the interaction alone. As a WIMP will interact only
 215 once in the detector, we remove events which have more
 216 than one S2. We adopt here a cut that is more suitable
 217 to higher energies and demands a single S2 in a $160 \mu\text{s}$
 218 window instead of a linear dependence between the second
 219 S2 size and the first one. To define the interaction's exact
 220 location, we use several algorithms, one of which is based
 221 on a Neural Network (NN) [18]. The NN was not trained
 222 to recognize high energy ER events and therefore a cut on
 223 the NN score is not suitable for this analysis. We do keep
 224 all other cuts on position reconstruction quality which are
 225 sufficient to ensure a correct position reconstruction.

226 The total acceptance to WIMP signals is computed
 227 based on $^{241}\text{AmBe}$ calibration data and follows the pro-
 228 cedure described in [18] as a function of $cS1$ and pre-
 229 sented in Figure 2, the total acceptance is fitted using a
 230 3rd order polynomial.

231 We define our signal region in the discrimination
 232 ($y, cS1$)-plane using $^{241}\text{AmBe}$ calibration data. The ROI

#	Band	Energy Range (cS1)	# Background Events	# Data Events
1	upper	30 - 40	23.5	20
2	upper	40 - 50	15.7	17
3	upper	50 - 80	12.4	11
4	upper	80 - 120	1.1	1
5	upper	120 - 150	0.1	1
6	upper	150 - 180	0.08	0
7	lower	30 - 50	0.9	0
8	lower	50 - 90	0.35	0
9	lower	120 - 180	0.18	0

TABLE I. Bins definition. The estimated background event is calculated by taking the calibration sample and scaling it by 6.54×10^{-3} , which is the ratio of data and calibration in a sideband.

is shown in Figure 3 as blue contour lines: the upper bound is defined such that it is not contaminated from contribution due to xenon excitation lines, the lower is defined as the 3σ acceptance quantile of the $^{241}\text{AmBe}$ distribution.

We divide our signal region into two bands, they are constructed such that the $^{241}\text{AmBe}$ data sample is equally distributed in y between them. The total number of events in a band is ~ 3000 events. The bands are further divided into nine bins. The definition and content of the bins are presented in table I and in Figure 3.

The main source of background results from ER leakage and hence, we estimate the background distribution in the ROI using ^{60}Co and ^{232}Th calibration samples. Contribution from radiogenic and cosmogenic neutrons, and accidental coincidence are negligible for such a high energy recoil. For illustration purposes we report in Table I the background expectation for each ROI bin along side with the observed data events. The background expectation is computed by scaling the calibration sample yield by 6.54×10^{-3} , which is merely the ratio of observed data and calibration in an independent sideband. Note that in the background normalization is fitted to data during hypothesis testing, as described in section III D.

C. Signal Model

The signal model is produced by taking a theoretical event rate spectrum, the production of which is described in sections III C 1 and III C 2, and applying the analysis acceptance and detector response as described in [20] to obtain the expected event rate in the detector in terms of detector variables (i.e. cS1,cS2). In order to calculate the expected value of the signal in cS1, we use Eq. 2 for both energy regions,

$$\langle cS1 \rangle = E_{nr} \cdot (L_y \mathcal{L}_{eff}) \cdot \left(\frac{S_{nr}}{S_{ee}} \right) \quad (2)$$

where E_{nr} is the recoil energy, L_y is the detector related light yield, \mathcal{L}_{eff} is the scintillation efficiency relative to

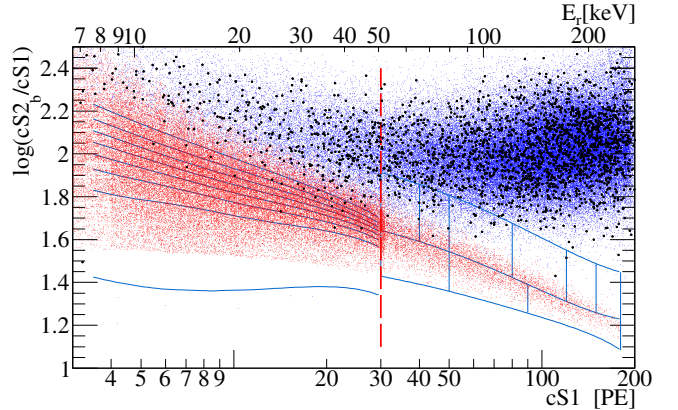


FIG. 3. ^{60}Co and ^{232}Th data in light gray and DM data in black dots. The red line is the threshold between the lowE part and the highE one. In blue are the bands. For the lowE constructed using data from a $50 \text{ GeV}/c^2$ WIMP. For the highE region the 9 bins are presented. top left is bin number 1, top right is bin number 6, bottom left is bin number 7 and bottom right is bin number 9.

122keV_{ee} as a function of E_{nr} , and S_{ee} and S_{nr} are the quenching factors for ER and NR respectively. Aside from E_{nr} and \mathcal{L}_{eff} these parameters have fixed values, namely $L_y = 2.28 \pm 0.04$, $S_{nr} = 0.95$, and $S_{ee} = 0.58$. Recoils below 3 keV are assumed to produce no light since \mathcal{L}_{eff} is not measured at these energies. For details of the physics behind these parameters and the construction of the signal PDF please see [7, 20].

The expected cS2 signal is computed following [21] using Eq. 3 for the lowE region only,

$$\langle cS2_{bottom} \rangle = E_{nr} Q_y Y \quad (3)$$

where $Y = 8.27 \pm 0.26$ is the amplification factor determined from the detector response to single electrons [22], and Q_y is the charge yield as a function of E_{nr} . Note that as some of the top PMTs saturate we use only the bottom PMT for energy scale in S2. Applying the detector and PMT responses, and the acceptance as in [7], defines the lowE signal model over the region $3\text{PE} < cS1 < 30\text{PE}$, with $cS2_b > 73.5\text{PE}$.

Eq. 3 hides a small subtlety. The actual $cS2_{bottom}$ PDF is composed of two pieces, a Poisson term associated with the initial charge liberation and a Gaussian term associated with the PMT response and other detector effects:

$$ps_2(cS2_b|E) = \sum_{N'} P_{pmt}(cS2_b|YN', \sigma_Y \sqrt{N'}). \text{Pois}(N'|\mu_Q) \quad (4)$$

where $\mu_Q = E_{nr} Q_y$ is the expected number of liberated charges in a nuclear recoil event of energy E , and N' is the actual number of liberated charges, which are unmeasured and thus summed over. The amplification factor Y is applied on the actual number of liberated charges N' , not the expected number μ_Q . Associated with this is the

297 variance of the Gaussian response PDF, $\sigma_Y \sqrt{N'}$, where
 298 in this analysis $\sigma_Y = 6.93$.

299 For the high energy region we can not produce the
 300 S2 distribution as the method in [21] is not calibrated
 301 for high enough recoil energies. We therefore use the
 302 NR calibration data distribution in $\log(cS2_b/cS1)$ to es-
 303 timate the WIMP one. Above 180PE in cS1 the statistics
 304 of $^{241}\text{AmBe}$ data is too low to estimate the distribution
 305 accurately so this forms the higher bound of this analy-
 306 sis. With the cS2_b distribution determined by this em-
 307 pirical method we require only a prediction of the cS1
 308 distribution. This is obtain from Eq. 2, followed by the
 309 application of detector and PMT responses, as well as the
 310 acceptance given in 2, which completes the highE signal
 311 model definition.

312 Examples of each for two EFT operators are shown
 313 in Figures 4 and 5, with the rate normalized to give 5
 314 events in the total energy range (lowE and highE).

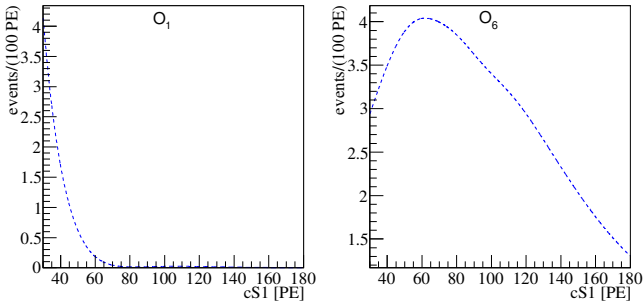


FIG. 4. The expected signal in the high energy region for a 300 GeV/c^2 WIMP mass, Normalized to 5 events. Left(right) is the spectra for $O_1(O_6)$. Notice that for O_1 most of the events are not expected to deposit energy higher than 30 PE whereas for O_6 a large fraction of the events appear in this region.

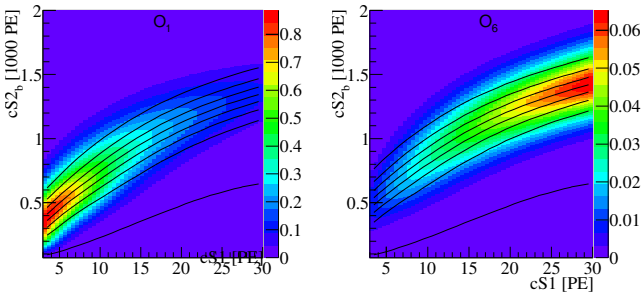


FIG. 5. The expected signal in the low energy region for a 300 GeV/c^2 WIMP mass, Normalized to 5 events. Left(right) is the spectra for $O_1(O_6)$. Notice that for O_1 most of the events are expected to deposit energy lower than 30 PE whereas for O_6 a large fraction of the events do not appear in this region at all. The black lines indicate the bands constructed on this specific event rate, and are dividing the signal into 8 equally distributed signal sub-regions.

1. Elastic Scattering

315 The expected recoil energy spectrum of each WIMP
 316 mass for each EFT operator is calculated using the Math-
 317 ematica package **DMFormFactor** supplied by Anand et.
 318 al. [12, 13]. We use standard assumptions as in previ-
 319 ous analyses (e.g [7]) regarding the local dark matter
 320 density and velocity distribution, namely $\rho_{\text{local}} = 0.3$
 321 GeV/cm^3 and a Maxwell-Boltzman distribution with a
 322 mean given by the local circular velocity $v_0 = 220 \text{ km/s}$
 323 and cut off at an escape velocity of $v_{\text{esc}} = 544 \text{ km/s}$.
 324 The responses of Xe nuclei to a scattering event are
 325 computed from one-body density matrices provided with
 326 the package, in contrast to the Helm form factors which
 327 have been used in previous analyses. These spectra
 328 are produced for the seven most abundant Xe isotopes
 329 (128,129,130,131,132,134 and 136), combined in propor-
 330 tion to the abundance of these isotopes in the experiment
 331 [23], then translated into expected signal rates via the
 332 method described above.

2. Inelastic WIMP Scattering

333 To obtain recoil spectra for WIMP-nucleon scattering
 334 for all EFT operators with inelastic kinematics, we use
 335 a modified version of **DMFormFactor** provided by Barello
 336 et. al. [15]. The authors have modified the original
 337 package to enforce the new energy conservation condi-
 338 tion $\delta_m + \vec{v} \cdot \vec{q} + |\vec{q}|^2 / 2\mu_N = 0$, primarily by replacing
 339 $\vec{v}_{\text{elastic}}^\perp \rightarrow \vec{v}_{\text{inelastic}}^\perp = \vec{v}_{\text{elastic}}^\perp + \frac{\delta_m}{|\vec{q}|^2} \vec{q}$ in the definitions of
 340 the EFT and nuclear operators, giving rise to the well-
 341 known minimum velocity for scattering

$$v_{\min} = \frac{1}{\sqrt{2m_N E_R}} \left| \frac{m_N E_R}{\mu_N} + \delta_m \right| \quad (5)$$

342 where μ_N is the WIMP-nucleon reduced mass.

343 Assumptions regarding the dark matter halo and nu-
 344 clear physics are unchanged. The mass splitting δ_m be-
 345 tween dark matter states is varied from 0 to 300 keV,
 346 safely beyond the value at which the predicted rate is
 347 zero for the entire mass range we consider.

D. Statistical Inference

348 The statistical interpretation of data is performed by
 349 means of a binned profiled likelihood approach, hypoth-
 350 esis testing rely on a likelihood ratio test statistic, \tilde{q} , and
 351 its asymptotic distributions [24]. The statistical com-
 352 bination between the two analysis channels is achieved
 353 merely by the product of the likelihood functions. Both
 354 analysis parametrize the NR relative scintillation effi-
 355 ciency, \mathcal{L}_{eff} , based on existing measurements [25], its un-
 356 certainty is the major contributor to energy scale un-
 357 certainties and considered as correlated between the two

analysis channels. Throughout this study, all the parameters related to systematic uncertainties are assumed to be normally distributed.

For the low energy channel an extended likelihood function is employed very similarly to what reported in [26] and described in detail in [7]. The ROI discriminating ($y, cS1$)-plane is divided into eight WIMP mass dependent bands where events are counted, this binned approach is extended with the corresponding $cS1$ -projected pdf of each band. The total normalization of the background is fit to data, and an uncertainty is assigned to the relative normalization of each band according to the corresponding statistical uncertainty of the calibration sample. Signal shape variations due to energy scale uncertainty are modeled via simulation, additionally to \mathcal{L}_{eff} , uncertainties due to the charge yield function, Q_y , are parametrized as described in [27].

The high energy channel analysis employs a binned likelihood function. Observed and expected event yield are compared in the nine ROI ($y, cS1$)-bins described in section III B. Given the large statistical uncertainty of the background model the above extended likelihood approach is not repeated here. The MLE of the background expectation in each bin is constrained by the statistical uncertainty of the calibration sample, while the total normalization is fit to the data. Additionally, to account for potential mismodeling of the expected background distribution, mainly due anomalous multiple scatter events, a systematic uncertainty of 20% is assigned independently to each bin. In this channel, uncertainty on the signal acceptance of analysis selections are computed for each signal hypothesis using the parametrized acceptance curve shown in Figure 2. Uncertainties on the signal model ($y, cS1$) distribution due to $^{241}\text{AmBe}$ sample statistical fluctuations, as well as energy scale shape variation due to \mathcal{L}_{eff} uncertainties are implemented.

IV. RESULTS

A benchmark region of interest is defined between the upper and lower thresholds in $cS1$ for each channel. This region is bounded in y space from above by the $^{241}\text{AmBe}$ NR mean line and below by the lower 3σ quantile of the AmBe neutron calibration data. The expected background in the region is 3 ± 0.5 (lowE) and 1.41 ± 0.28 (highE). The number of DM candidates recorded in this region is 3 (lowE), and 0 (highE). The data is compatible with background only hypothesis and no excess is found.

For the elastic scattering case, a 90% CL_s [28] confidence level limit is set on the effective coupling constant, c_i , for all operators and masses in the range of $10 \text{ GeV}/c^2$ to $1 \text{ TeV}/c^2$. These limits are shown in Fig. 7 in black, along with the limits from CDMS-II Si, CDMS-II Ge and SuperCDMS [29]. For operators 3 and 8, a full CDMS limit is presented, for all other operators only the limit for a $10 \text{ GeV}/c^2$ and $300 \text{ GeV}/c^2$ are published.

For the inelastic scattering case, 90% CL_s confidence

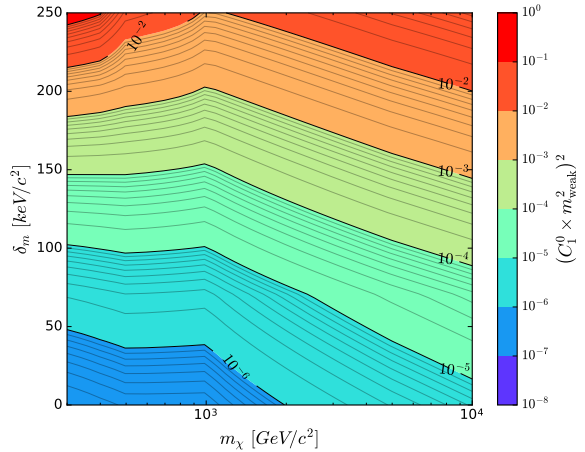


FIG. 6. 90% confidence level limits on coupling constant for \mathcal{O}_1 reported as a function of the WIMP mass and mass splitting δ_m .

level limits on the coupling constant are set. Fig. 6 shows limits on the SI (operator \mathcal{O}_1) coupling constant as a function of mass splitting and WIMP mass, whereas Fig. 8 shows limits for all other operators as a function of the mass splitting δ_m and for a WIMP mass of $1 \text{ TeV}/c^2$.

V. SUMMARY

We have shown the first analysis in XENON100 looking at energy recoils above 43 keV extending the high energy bound to 240 keV. We considered in this paper two models which predicts interactions in that energy region, an EFT approach for elastic WIMP nucleon scattering, and inelastic WIMP nucleon scattering. The data was compatible with background expectations, and 90% exclusion limits were constructed, setting the strongest limit for these models, for WIMP masses between 10-1000 GeV.

VI. ACKNOWLEDGMENT

Liam Fitzpatrick Spencer Chang

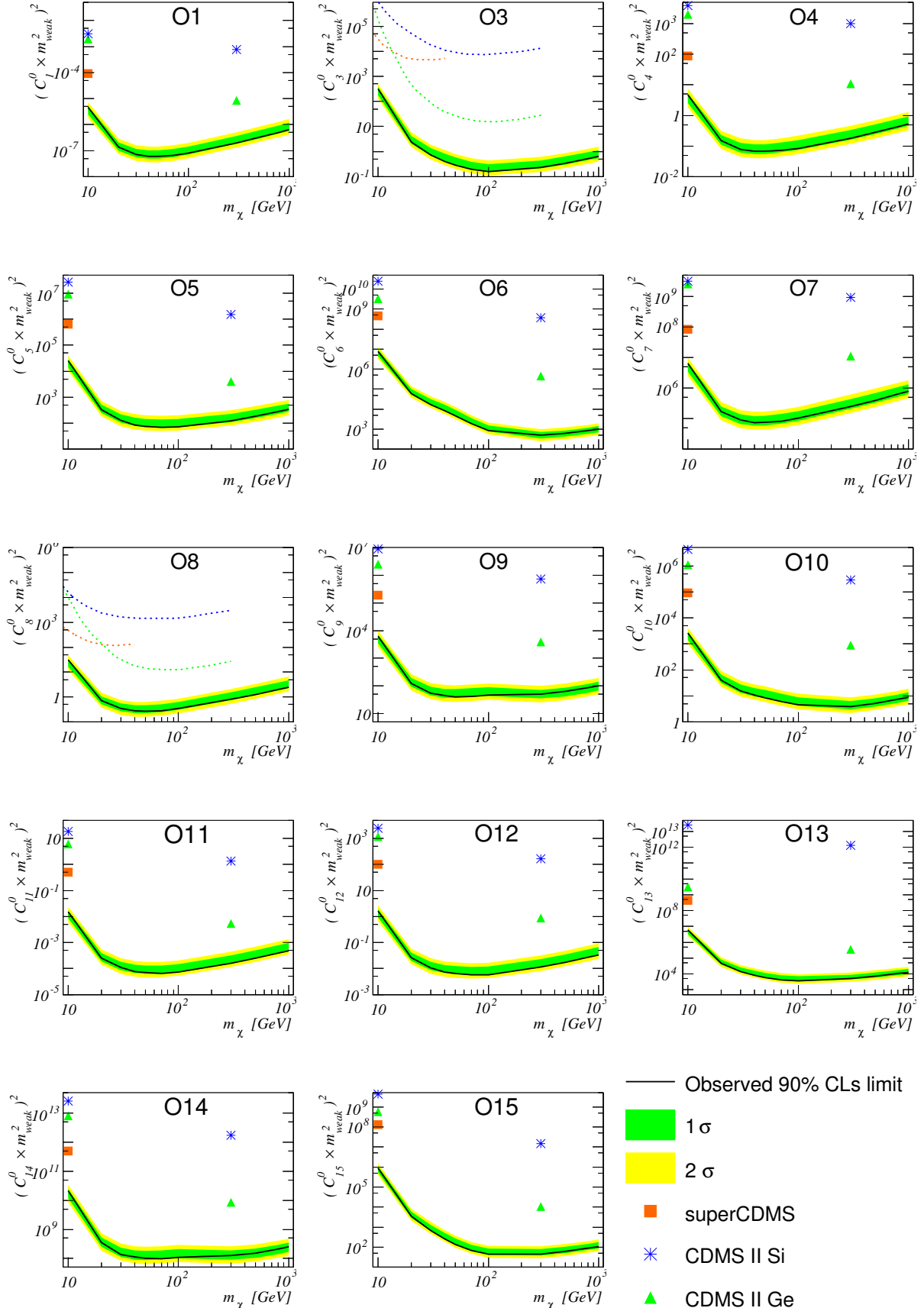


FIG. 7. The XENON100 limits (90% CL) Limits on isoscalar dimensionless coupling for all elastic scattering EFT operators are indicated in solid black. The expected sensitivity obtained assuming background only are shown in green and yellow(1σ and 2σ respectively). Limits from CDMS-II Si CDMS-II Ge and SuperCDMS citeCDMS are presented in blue Asterix ,green triangle and orange rectangle (color online). For operator 3 and 8 a full limit from CDMS is published and indicated by a dashed line in the respected colors.

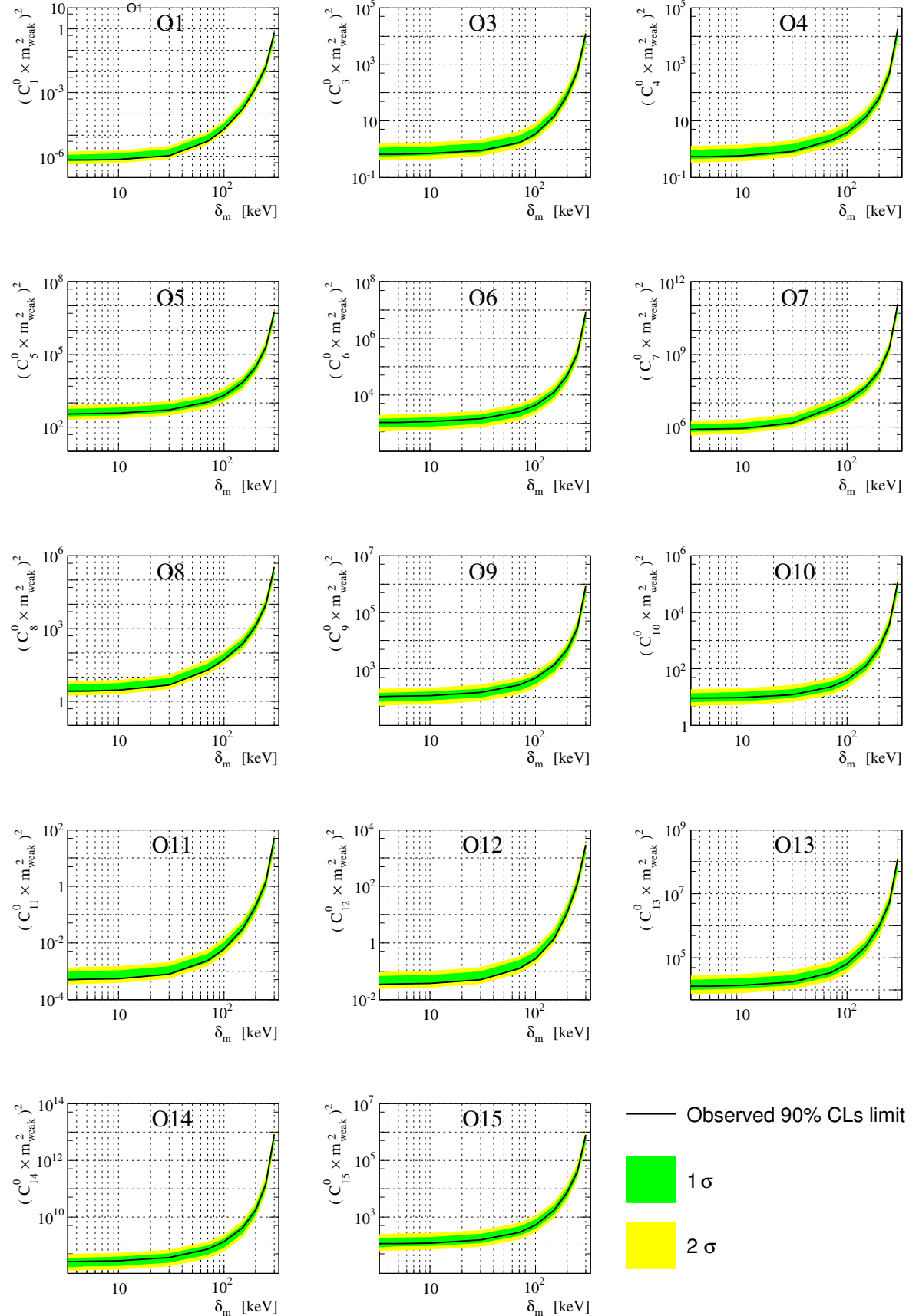


FIG. 8. The XENON100 limits (90% CL) Limits on a $1 \text{ TeV}/c^2$ WIMP isoscalar dimensionless coupling for all inelastic scattering EFT operators are indicated in solid black. The expected sensitivity obtained assuming background only are shown in green and yellow (1σ and 2σ respectively).

434 Appendix A: Signal model detector response table

435 In this appendix we describe digital tables which can
 436 be used to construct an accurate signal model for this
 437 analysis given any input recoil spectrum dR/dE . A vi-
 438 sualisation of the tables is shown in Fig. 9, and in section
 439 A 1 we show a simple example of how to use the supplied
 440 tables in Python. Currently we provide these tables only
 441 for the high E analysis region.

The signal model for the high E analysis region can be expressed analytically in the form:

$$\frac{dR}{dcS1} = \int \frac{dR}{dE} \cdot \epsilon_{S1}(cS1) \cdot \epsilon_{S2'}(E) \cdot p_{S1}(cS1|E) dE \quad (A1)$$

$$= \int \frac{dR}{dE} G(cS1, E) dE \quad (A2)$$

442 where $\epsilon_{S1}(cS1)$ and $\epsilon_{S2'}(E)$ represent analysis cut effi-
 443 ciencies, $p_{S1}(cS1|E)$ encodes detector effects, and dR/dE
 444 gives the theoretically predicted nuclear recoil rate from
 445 WIMP scattering. In the second line we emphasise that
 446 all the detector and analysis effects can be encoded in a
 447 single function $G(cS1, E)$. To make a signal prediction
 448 for the bins in our analysis this expression needs to be
 449 integrated over the appropriate range of $cS1$ for each bin
 450 (and divided by two to account for the banding structure
 451 in $cS2_b$):

$$R_{\text{bin}_i} = \frac{1}{2} \int_{\text{lower}_i}^{\text{upper}_i} \frac{dR}{dcS1} dcS1 \quad (A3)$$

With some simple rearrangement this rate can be written in terms of an integral over the detector response function G as follows

$$R_{\text{bin}_i} = \frac{1}{2} \int \frac{dR}{dE} \int_{\text{lower}_i}^{\text{upper}_i} G(cS1, E) dcS1 dE \quad (A4)$$

$$= \int \frac{dR}{dE} G'_i(E) dE \quad (A5)$$

452 where in the last line we absorb the factor of 1/2 into
 453 the definition of G'_i . We see here that the signal rate for
 454 each bin can be expressed as an integral over the recoil
 455 spectrum times a detector response function G'_i for that
 456 bin. It is these detector response functions which are
 457 shown in Fig. 9, and which we provide digitally for use by
 458 the community. With these tables it is simple to produce
 459 a signal model for our analysis for any input theoretical
 460 recoil spectrum. The functions G'_i are provided for three
 461 values of the nuisance variable \mathcal{L}_{eff} , namely the median
 462 value and values at $\pm 1\sigma$ in \mathcal{L}_{eff} . From these, along with
 463 the measured background rates given in table I, one may
 464 construct a likelihood which accounts for uncertainties in
 465 \mathcal{L}_{eff} , however simply using the -1σ value produces quite
 466 an accurate prediction and is generally conservative.

467 Details of how to extract and use the provided G' func-
 468 tions are given in the example of section A 1.

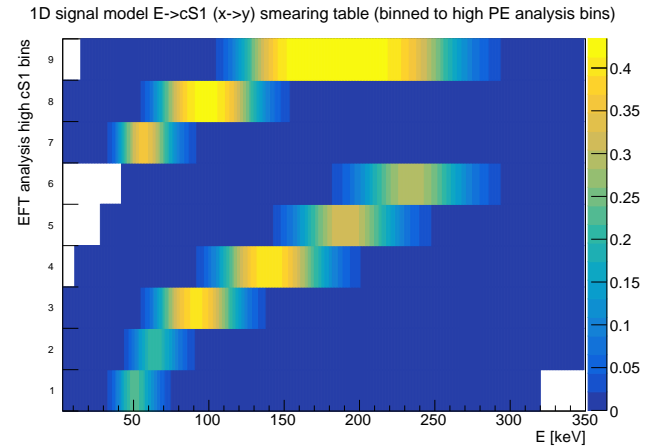


FIG. 9. A visualisation of the detector response table for -1σ (i.e. conservative) \mathcal{L}_{eff} , as provided in the supplementary material. The table visualisation shows, on the y axis, the bins used for the high E signal region of this analysis. The x axis shows recoil energies, and the colours give the probability density for a recoil of a given recoil energy to produce an event in each analysis bin. To produce a signal model for this analysis, one simply multiplies the table values by dR/dE and integrates over E . The result is the predicted signal rate for each analysis bin.

#	E (keV)	bin 1	bin 2	...	bin 9
3.00e+00	1.44e-22	2.70e-32	1.23e-42	0.00e+00	0.00e+00
1.30e+01	9.21e-09	7.58e-14	1.25e-19	6.21e-40	0.00e+00
2.30e+01	1.74e-04	1.07e-07	1.24e-11	1.51e-26	0.00e+00
3.30e+01	2.22e-02	2.79e-04	6.56e-07	5.47e-18	8.20e-38
4.30e+01	1.59e-01	1.68e-02	3.50e-02	1.89e-12	1.24e-28
5.30e+01	2.23e-01	1.21e-01	1.40e-02	1.28e-08	6.89e-22
6.30e+01	1.10e-01	2.12e-01	9.84e-02	4.73e-06	5.28e-17
7.30e+01	2.77e-02	1.54e-01	2.51e-01	2.58e-04	2.20e-13
8.30e+01	4.38e-03	6.14e-02	3.67e-01	4.07e-03	1.36e-10
9.30e+01	4.65e-04	1.52e-02	3.96e-01	2.73e-02	2.31e-08
1.03e+02	3.40e-05	2.47e-03	3.41e-01	9.81e-02	1.50e-06
1.13e+02	1.91e-06	2.89e-04	2.29e-01	2.13e-01	4.09e-05
1.23e+02	7.75e-02	2.38e-05	1.14e-01	3.28e-08	5.91e-04
1.33e+02	2.18e-09	1.33e-06	3.98e-02	3.97e-01	5.03e-06
1.43e+02	5.40e-11	6.21e-08	1.05e-02	4.06e-01	2.41e-02
1.53e+02	1.33e-12	2.71e-09	2.23e-03	3.66e-02	7.14e-04
1.63e+02	2.86e-14	1.00e-10	3.75e-04	2.85e-01	1.51e-01
1.73e+02	5.43e-16	3.19e-12	5.09e-05	1.86e-01	2.43e-01
1.83e+02	9.29e-18	8.90e-14	5.69e-06	1.01e-01	3.09e-02
1.93e+02	1.44e-19	2.21e-15	5.32e-07	4.46e-02	8.90e-16
2.03e+02	2.05e-21	4.92e-17	4.23e-08	1.62e-02	2.83e-01
2.13e+02	2.71e-23	9.96e-19	2.91e-08	4.89e-03	2.10e-01
2.23e+02	3.33e-25	1.85e-20	1.74e-10	3.03e-01	1.31e-01
2.33e+02	3.83e-27	3.16e-22	2.95e-12	2.63e-04	6.94e-02
2.43e+02	4.16e-29	5.03e-24	4.38e-14	4.80e-05	3.12e-02
2.53e+02	4.29e-31	7.48e-26	1.87e-14	7.55e-06	1.20e-02
2.63e+02	4.21e-33	1.05e-27	2.73e-16	1.04e-06	3.94e-03
2.73e+02	3.95e-33	1.39e-29	2.56e-17	1.25e-07	1.12e-03
2.83e+02	3.56e-37	1.74e-31	8.33e-19	1.34e-08	2.77e-04
2.93e+02	3.08e-39	2.08e-33	2.51e-19	6.00e-06	2.31e-02
3.03e+02	2.58e-41	2.38e-35	7.04e-22	1.11e-10	1.15e-05
3.13e+02	2.03e-43	2.61e-37	1.84e-23	8.69e-12	1.95e-06
3.23e+02	0.00e+00	2.76e-39	4.54e-26	6.20e-13	2.97e-07
3.33e+02	0.00e+00	2.81e-41	1.05e-26	4.06e-14	4.06e-08
3.43e+02	0.00e+00	2.72e-43	2.32e-28	2.44e-15	5.04e-09

FIG. 10. Detector response table using \mathcal{L}_{eff} with constrained scaling parameter set to -1σ value. First column gives recoil energies, subsequent columns give the values of $G'_i(E)$ for each of the 9 high E analysis bins. The sampling is in steps of 10 keV, which is too coarse to give an accurate signal model for very low WIMP masses, but is suitable for the mass range most relevant to our analysis. Higher resolution $G'_i(E)$ functions, and $G'_i(E)$ functions for other values of \mathcal{L}_{eff} , are given in supplementary material(give URL).

 469 1. Example code

```

470
471 import numpy as np
472 from numpy import newaxis
473 from scipy.interpolate import interp1d
474
475 def TrapI(x,y):
476     """Simple trapezoid integration"""
477     w = x[1:] - x[:-1]
478     h = (y[1:] + y[:-1])/2.
479     return np.sum(w*h, axis=0)
480
481 # Load detector response table
482 data = np.loadtxt("detector_table.dat")
483 E = data[:,0]; Gi = data[:,1:]
484
485 # Load test recoil spectrum (1 TeV WIMP, 06)
486 data = np.loadtxt("06_1TeV.dat")
487 Er = data[:,0]
488 # Input spectra is normalised to coupling^2=1,
489 # rescale to something near limit (1e3)
490 # Also multiply in the appropriate exposure

```

```

491 dRdE = data[:,1] * (1e3/1.) * 224.6*34.
492
493 # Interpolate recoil spectrum to table values
494 # Assume spectrum zero outside data given
495 f_dRdE = interp1d(Er,dRdE)
496 dRdE_matched = f_dRdE(E)
497 Ri = TrapI(E[:,newaxis],Gi*dRdE_matched[:,newaxis])
498
499 for i,R in enumerate(Ri):
500     print "bin {0}: rate = {1:.2g}".format(i+1,R)

```

502 Output:

```

503
504 bin 1: rate = 0.081
505 bin 2: rate = 0.098
506 bin 3: rate = 0.35
507 bin 4: rate = 0.46
508 bin 5: rate = 0.29
509 bin 6: rate = 0.22
510 bin 7: rate = 0.18
511 bin 8: rate = 0.47
512 bin 9: rate = 0.84

```

- 514 [1] David Harvey, Richard Massey, Thomas Kitching, Andy 550 tering response. *Phys. Rev.*, C89(6):065501, 2014.
- 515 Taylor, and Eric Tittley. The nongravitational interac- 551 [13] A. Liam Fitzpatrick, Wick Haxton, Emanuel Katz,
516 tions of dark matter in colliding galaxy clusters. *Science*, 552 Nicholas Lubbers, and Yiming Xu. The Effective
517 347(6229):1462–1465, 2015. 553 Field Theory of Dark Matter Direct Detection. *JCAP*,
554 1302:004, 2013.
- 518 [2] J. Silk et al. *Particle Dark Matter: Observations, Models 555 [14] David Tucker-Smith and Neal Weiner. Inelastic dark
519 and Searches*. Cambridge Univ. Press, Cambridge, 2010. 556 matter. *Phys. Rev.*, D64:043502, 2001.
- 520 [3] R. Bernabei et al. New results from dama/libra. *The 557 [15] G. Barello, Spencer Chang, and Christopher A. Newby.
521 European Physical Journal C*, 67(1):39–49, 2010. 558 A Model Independent Approach to Inelastic Dark Matter
522 [4] C. E. Aalseth et al. Cogent: A search for low-mass dark 559 Scattering. *Phys. Rev.*, D90(9):094027, 2014.
- 523 matter using p -type point contact germanium detectors. 560 [16] E. Aprile et al. The XENON100 Dark Matter Experi-
524 *Phys. Rev. D*, 88:012002, Jul 2013. 561 ment. *Astropart. Phys.*, 35:573–590, 2012.
- 525 [5] R. Agnese et al. Search for low-mass weakly interact- 562 [17] E. Aprile et al. Dark Matter Results from 225 Live Days
526 ing massive particles using voltage-assisted calorimetric 563 of XENON100 Data. *Phys. Rev. Lett.*, 109:181301, 2012.
- 527 ionization detection in the supercdms experiment. *Phys. 564 [18] E. Aprile et al. Analysis of the XENON100 Dark Matter
528 Rev. Lett.*, 112:041302, Jan 2014. 565 Search Data. *Astropart. Phys.*, 54:11–24, 2014.
- 529 [6] G. and others Angloher. Results from 730 kg days of the 566 [19] E. Aprile et al. The neutron background of the
530 cresst-ii dark matter search. *The European Physical Jour- 567 XENON100 dark matter search experiment. *J. Phys.*,
531 nal C*, 72(4):1971, 2012. 568 G40:115201, 2013.
- 532 [7] E. Aprile et al. XENON100 Dark Matter Results 569 [20] E. Aprile et al. *Astropart. Phys.*, 11:54, 2014.
- 533 from a Combination of 477 Live Days. *Phys. Rev.*, 570 [21] E. Aprile et al. Response of the XENON100 Dark Matter
534 D94(12):122001, 2016. 571 Detector to Nuclear Recoils. *Phys. Rev.*, D88:012006,
535 [8] Andi Tan and otrhers. Dark matter results from first 98.7 572 2013.
- 536 days of data from the pandax-ii experiment. *Phys. Rev.* 573 [22] E. Aprile et al. Observation and applications of single-
537 *Lett.*, 117:121303, Sep 2016. 574 electron charge signals in the XENON100 experiment. *J.*
538 [9] D. S. Akerib et al. Improved Limits on Scattering of 575 *Phys.*, G41:035201, 2014.
- 539 Weakly Interacting Massive Particles from Reanalysis of 576 [23] E. Aprile et al. Limits on spin-dependent wimp-nucleon
540 2013 LUX Data. *Phys. Rev. Lett.*, 116(16):161301, 2016. 577 cross sections from 225 live days of xenon100 data. *Phys-
541 [10] J. D. Lewin and P. F. Smith. Review of mathematics, 578 ical review letters*, 111(2):021301, 2013.
- 542 numerical factors, and corrections for dark matter exper- 579 [24] Glen Cowan, Kyle Cranmer, Eilam Gross, and Ofer
543 iments based on elastic nuclear recoil. *Astropart. Phys.*, 580 Vitells. Asymptotic formulae for likelihood-based tests
544 6:87–112, 1996. 581 of new physics. *Eur. Phys. J.*, C71:1554, 2011. [Erratum:
545 [11] A. Liam Fitzpatrick, Wick Haxton, Emanuel Katz, 582 Eur. Phys. J.C73,2501(2013)].
- 546 Nicholas Lubbers, and Yiming Xu. Model Independent 583 [25] E. Aprile et al. Dark Matter Results from 100 Live Days
547 Direct Detection Analyses. 2012. 584 of XENON100 Data. *Phys. Rev. Lett.*, 107:131302, 2011.
- 548 [12] Nikhil Anand, A. Liam Fitzpatrick, and W. C. Haxton. 585 [26] E. Aprile et al. Likelihood Approach to the First
549 Weakly interacting massive particle-nucleus elastic scat-

- 586 Dark Matter Results from XENON100. *Phys. Rev.*, 592
587 D84:052003, 2011.
588 [27] E. Aprile et al. Response of the XENON100 Dark Matter 593
589 Detector to Nuclear Recoils. *Phys. Rev.*, D88:012006, 594
590 2013.
591 [28] Alexander L. Read. Modified frequentist analysis of 595
596
597 search results (The CL(s) method). In *Workshop on con-*
598 fidence limits, CERN, Geneva, Switzerland, 17-18 Jan
599 2000: Proceedings, pages 81–101, 2000.
[29] K. Schneck et al. Dark matter effective field theory
scattering in direct detection experiments. *Phys. Rev.*,
D91(9):092004, 2015.